



Dynamic orientation transition of the lyotropic lamellar phase at high shear rate

Journal:	<i>Soft Matter</i>
Manuscript ID	SM-ART-07-2015-001755.R1
Article Type:	Paper
Date Submitted by the Author:	05-Sep-2015
Complete List of Authors:	Fujii, Shuji; Nagaoka University of Technology, Yamamoto, Yuki; Nagaoka University of Technology,

Dynamic orientation transition of the lyotropic lamellar phase at high shear rate

Shuji Fujii,* and Yuki Yamamoto

The dynamic orientation behavior of the lamellar phase of a triblock copolymer is studied under a wide range of shear rate as a function of solvent composition. We find that various phases can be induced by increasing the shear rate. At low shear rate, the onion phase forms from planar lamellae with many defects. Further increase of the shear rate caused the onion structure to break down, and the lamellar phase recovers with fewer defects. Finally, the transition of the orientation from parallel to perpendicular is observed at high shear rate. In the orientation transition at high shear rate, a stable intermediate structure, to our knowledge, is found for the first time. We also find that the critical shear stress of the rupture of the onion phase coincides with the orientation transition. The consistency of the critical shear stress suggests that all orientation transitions at a high shear rate are dominated by a mechanical balance between applied viscous stress and the internal relaxation mode of the lamellae.

1 Introduction

Layered systems such as amphiphilic lamellar phase and thermotropic smectic phase show fascinating non-equilibrium phase transitions under shear flow^{1–24}. The lyotropic lamellar phase shows two kinds of non-equilibrium structural transitions. One of these transitions is a shear-induced multilamellar vesicle phase, which has been reported for many surfactant lamellar phases^{1–15}. Because of its unique structure, multilamellar vesicles are referred to as onion phases. Onion phases are produced from planar lamellae by shearing and are thermodynamically stable. During the formation of the onion phase, a concentric multilamellar cylinder structure resembling a leek forms as a transient intermediate structure^{4,5}. The second non-equilibrium structural transition is a shear-induced orientation transition of layers^{14,15,19,20}. In this orientation transition, the orientation direction of the layer normal changes from parallel to perpendicular relative to the velocity gradient direction at the critical shear rate. The dynamic orientation transition is a phenomenon common to all layered systems. The orientation transition can also be seen in polymer melt systems^{21–24}, although the detailed mechanism is not the same due to polymeric features such as entanglement and asymmetric viscoelasticity between layers. Most orientation diagrams of lyotropic lamellar systems describe either onion phase formation or orientation transition; only a few systems are known to show both transitions with change in sample composition and shear rate^{13,20}.

The origin of the above structural transitions have been discussed for more than two decades. However, some issues are yet unsolved. For example, the critical conditions for these transitions, the role of the elastic properties of the lamellae, the existence of a stable intermediate structure, and the conditions for rupture of the onion structure at high shear rate

remain unknown. Furthermore, the major questions of how the most favorable structure is chosen and what determines it are still unanswered. To date, several models have been proposed for the shear-induced instability of the lyotropic lamellar phase^{25–31}. Among them, only a few models explain the origin of the shear-induced onion phase formation. The Zilman-Granek model proposes the coupling of shear flow and the short wavelength undulations of membranes²⁸. In general, the undulation repulsive force is responsible for the stability of the lamellar phase. Thus the suppression of the membrane undulations due to shear flow induces instability and generates an effective dilatation. When the dilatation exceeds the critical value, the coherent buckling of the lamellar membranes occurs and the onion phase is formed. The other mechanism is primarily based on the work of Oswald and considers the motion of defects. Dislocations in the lamellar phase can move with the flow by permeation at a low shear rate²⁹. However, the permeation process is too low to allow dislocations to flow at high shear rates. Therefore, a delay in the dislocations against the shear flow generates dilative and compressive strain. In this model, the non-uniform shear flow due to the low mobility of the defects is the origin of the undulation instability, which results in the formation of the onion phase. The qualitative explanation for onion phase formation reported by Roux *et al.* is similar to this model^{1,2}. Interestingly, the common origin of the instability in both proposed mechanisms is dilative strain.

The effect of dilatation on the sheared lamellar phase also plays an important role in the orientation transition at high shear rates^{25–27,31}. Ramaswamy argued that the orientation transition is induced by the suppression of the undulations, as in the Zilman-Granek model. In addition, the rupture of the onion structure at high shear rate observed by Roux *et al.* can also be explained by considering the coupling of the flow and dilatation induced undulation instability (Wunenburger *et al.*). Recently, Lu described the scaling behavior of the size of the onion phase by considering the baroclinic mode, which

* Department of Materials Science and Technology, Nagaoka University of Technology, Nagaoka 940-2188, Japan. E-mail: sfujii@mst.nagaokaut.ac.jp

is induced by the solvent between layers and also by a shape relaxation of the onion structure³². The relaxation rate of the baroclinic mode is similar to that of the lamellar phase. In Lu's theory, the free energy minima of the dynamic free energy of lamellae determine the onion size, and the rupture of the onion phase at high shear rates can be well described by the disappearance of the free energy minima.

Although the undulation instability seems to play an important role in both structural transitions, why these different structural transitions take place at markedly different shear rates despite their common physical origin remains unclear. In addition, what controls the non-equilibrium phase transition and which non-equilibrium phase is the most favorable under shear are still unknown. In particular, details on the dynamic orientation transitions (e.g., the orientation transition and the rupture of the onion structure at high shear rates) are poorly understood compared with the onion formation behavior at low shear rate.

In this study, we focus on the structural and orientation transitions at high shear rates. We construct a dynamic orientation diagram using of rheo-physical methods such as viscometry, birefringence, and small-angle scattering under shear. Section 2 describes the materials and experimental methods used in this study. In Section 3, we show the data set obtained from those methods and identify the dynamic orientation state as a function of sample composition and shear rate. We also show the dynamic orientation diagram at several temperatures. We find that planar lamellae are reformed as the result of the rupture of the onion phase at high shear rates followed by the orientation transition of the lamellae. We also characterize the reformation of the planar lamellae after the rupture of the onion phase using a shear quench experiment. Section 4, we show that the rupture of the onion structure and reorientation transition appear at the same shear stress and discuss the mechanism of the orientation transition at high shear rates. We also discuss the presence of a stable intermediate structure in the orientation transition. We summarize our findings in Section 5.

2 Experimental

2.1 Sample preparation

We used a ternary lyotropic lamellar phase composed of amphiphilic triblock copolymers, Butanol and distilled water. **The amphiphilic triblock copolymer, poly(ethylene oxide)-b-poly(propylene oxide)-b-poly(ethylene oxide) (trade name Pluronic P123) was obtained from BASF and used as received.** This triblock copolymer comprised two hydrophilic ethylene oxide (EO) blocks bound to a central hydrophobic propylene oxide (PO) block. The degree of polymerization of the hydrophilic EO block is $N_{EO} \approx 20$, and the degree of polymer-

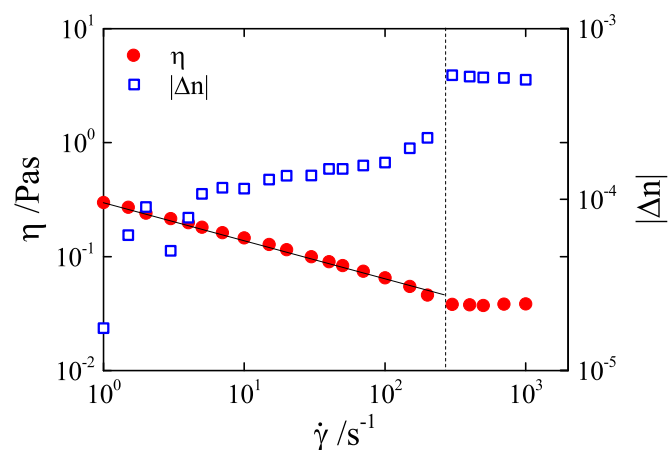


Fig. 1 Viscosity and birefringence intensity as a function of shear rate for the sample with $B/H=0.30$ at $25\text{ }^{\circ}\text{C}$. The vertical dotted line indicates the characteristic shear rate where the sample undergoes the layer orientation transition from parallel to perpendicular. **The solid line shows the power law relation, $\eta \sim \dot{\gamma}^{-1/3}$.**

ization of PO chains is $N_{PO} \approx 70$. **This system was chosen since the lamellar region is formed at rather low block copolymer concentrations³³. It has already been observed that the solution with an intermediate block copolymer concentration shows the orientation transition; for the same system at low concentration, the onion phase was observed, to our knowledge, for the first time in a lamellar block copolymer system¹³.** The prescribed amount of block copolymer and Butanol were dissolved into distilled water and gently stirred by a magnetic stirrer for 2 days. In this study, the concentration of Pluronic P123 was fixed at 23 wt%, and the solvent composition (i.e., the ratio of butanol to water, B/H) was controlled in the range of 0.3 to 0.4. **At a polymer concentration of 23 wt%, the lamellar phase is formed in wide range of B/H ³³.** Butanol plays the role of a cosurfactant; thus, most of the butanol is located at the interface between the hydrophilic and hydrophobic parts¹³. In all measurements, the sample was always cooled until the lamellar phase transitioned into an isotropic phase with low viscosity. The sample in the isotropic phase was loaded on the sample cell. Then, the temperature was set to the measurement condition and we waited for 1200 s.

2.2 Methods

Viscosity measurements were performed using an ARES-G2 strain-controlled rheometer (TA Instrument Co., Ltd.) with a couette geometry (height of bob=13 mm, gap size=250 μm). **During the viscosity measurements, shear rates ranging from**

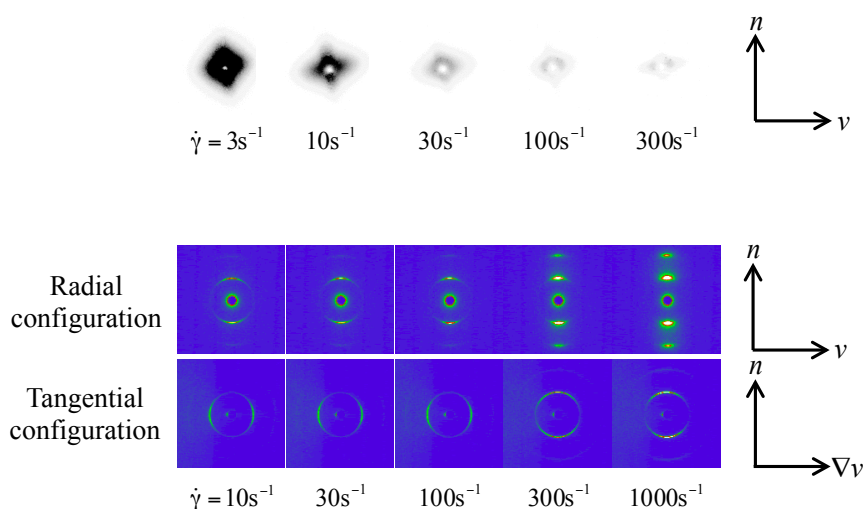


Fig. 2 Rheo-SALS (upper) and rheo-SAXS (bottom) patterns obtained for the same system shown in Fig. 1. In the rheo-SALS pattern, the vertical and horizontal directions correspond to the neutral (n) and flow (v) directions, respectively. In the rheo-SAXS pattern, scattering profiles in the neutral (n)-flow (v) plane (radial configuration) and the neutral (n)-velocity gradient (∇v) plane (tangential configuration) are shown. The shear rate corresponding to each images is shown at the bottom of images.

$\dot{\gamma}=1-1000 \text{ s}^{-1}$ were applied. Transient viscosity was measured at each shear rate until it reached steady state value. Depolarized small-angle light scattering measurements under shear (Rheo-SALS) were performed using a stress controlled rheometer (Anton Paar MCR-301) equipped with a quartz plate/plate shear geometry. The gap size between plates was fixed at $250 \mu\text{m}$, corresponding to the viscosity measurements³⁴. The incident beam of the He-Ne laser ($\lambda=658\text{nm}$) was polarized along the flow direction, and the analyzer was aligned perpendicular to the flow direction. The rheo-SALS pattern projected on a screen was recorded by a CCD camera. Flow birefringence measurements were also performed using the same rheometer as in rheo-SALS. The He-Ne laser ($\lambda = 633 \text{ nm}$) was incident on the sample along the velocity gradient direction and transmitted light was detected by a photodiode. In these rheo-optics measurements, shear rates in the range of $\dot{\gamma}=1-2000 \text{ s}^{-1}$ were applied. The SALS pattern and flow birefringence intensity were recorded after the viscosity reached a steady state value.

Small angle X-ray scattering (rheo-SAXS) measurements were conducted using synchrotron radiation at beam line BL-10C of the Photon Factory at the Institute of Materials Structure Science of the High Energy Accelerator Research Organization in Tsukuba, Japan³⁵. The scattering vector was defined as $q = (4\pi/\lambda) \sin(\theta/2)$, where θ and λ are the scattering angle and the wavelength in the medium, respectively. A self-made shear cell with couette geometry driven by a stepping motor was equipped on the beam line. The gap of the couette

shear cell is 1 mm . In this setup, shear rates in the range of $\dot{\gamma}=10-1500 \text{ s}^{-1}$ can be applied. SAXS images were obtained after the shear rate was applied for 600 s . Two scattering configurations were used in the rheo-SAXS measurements; a radial configuration where the beam passes the sample along the velocity gradient direction, allowing the 2D scattering pattern in the flow-neutral plane to be obtained, and a tangential configuration where the beam passes along the flow direction. Thus, the scattering pattern in the velocity gradient-neutral plane can be observed¹⁴.

Microscope observation under shear was performed using a Linkam shear cell (CSS450), which has a plate-plate shear geometry. The shear cell was attached onto an Olympus microscope (BX-50) and positioned between two polarizers. Sample thickness was kept at $250 \mu\text{m}$.

3 Non-equilibrium orientation

3.1 Identification of the lamellar orientation

Figure 1 shows the viscosity η and flow birefringence intensity $|\Delta n|$ as functions of the shear rate for the sample with $B/H = 0.30$ at $T = 25 \text{ }^\circ\text{C}$. Rheo-SALS and rheo-SAXS patterns at different shear rates for the same system are shown in Fig. 2. The same data sets for the sample with $B/H = 0.34$ are also shown in Figs. 3 and 4. At $B/H = 0.30$, the viscosity shows shear-thinning behavior over a wide shear rate region, which is a representative rheological behavior of the lyotropic lamellar

phase^{36–38}. The shear-thinning behavior follows a power law $\eta \sim \dot{\gamma}^{-1/3}$ in which the exponent corresponds to the theoretical prediction by Lu *et al.*³⁸. In the shear-thinning region, the birefringence intensity slightly increases with the shear rate. At $\dot{\gamma} = 300 \text{ s}^{-1}$, the shear-thinning viscosity shifts to Newtonian behavior. At the same shear rate as this rheological shift, $|\Delta n|$ suddenly increases and becomes saturated.

These shifts in the rheological and optical features indicate a structural transition of the lamellar phase. The dynamic orientation state of the lamellae was confirmed by the use of rheo-SALS and rheo-SAXS measurements. In the rheo-SALS pattern at low shear rate, diamond shaped scattering is observed. This diamond-like scattering is attributed to oily streak defects, a typical texture in the lamellar phase³⁹, as we will show in Fig. 5. The diamond pattern disappears with increasing shear rate, and no characteristic scattering is recognized at rates above $\dot{\gamma} = 30 \text{ s}^{-1}$, indicating that no specific mesoscale structure such as the onion phase is present. Unlike rheo-SALS, rheo-SAXS is sensitive to the layer orientation and reveals a characteristic feature related to the shifts in rheological and optical behavior. In the shear-thinning region ($\dot{\gamma} < 300 \text{ s}^{-1}$), SAXS patterns in the radial and tangential configurations show Bragg peaks along the neutral (n) and velocity gradient (∇v) directions, respectively. Lamellae stacked along the ∇v direction yield scattering peak along the same direction in the tangential configuration. This profile, the so-called c -orientation, is typical of the parallel-oriented lamellar phase¹³. The Bragg peak observed in the radial configuration is attributed to the undulating layers along the neutral direction. The same scattering profile was observed for the smectic liquid crystalline 8CB system with c -orientation in the couette cell¹⁸. We thus identify the orientation state in the shear-thinning region as c -orientation, referred to as the $L_\alpha(C)$ phase. However, when the shear-thinning behavior changes to Newtonian, the SAXS pattern of both configuration show remarkable changes. In the radial configuration, a new secondary peak appears, and peak intensity increases with the shear rate. In the tangential configuration, the direction of the Bragg peak drastically changes by 90° from the ∇v direction to the n direction. The Bragg peak along the n direction in the tangential configuration indicates that the lamellae are stacked in the n direction. Lamellae stacked along the n direction with high degrees of layer orientation can also induce the secondary peak in the pattern of the radial configuration. Since the orientation direction of the layer normal is perpendicular to the ∇v direction, the lamellar phase with this orientation is referred as a perpendicular orientation (i.e., the so-called a -orientation). In this study we refer to this orientation as the $L_\alpha(A)$ phase. These scattering profiles indicate the occurrence of the orientation transition of the lamellae from the $L_\alpha(C)$ phase to the $L_\alpha(A)$ phase. The orientation transition to the $L_\alpha(A)$ phase is reasonably coincidental with the jump in $|\Delta n|$ at $\dot{\gamma} = 300 \text{ s}^{-1}$.

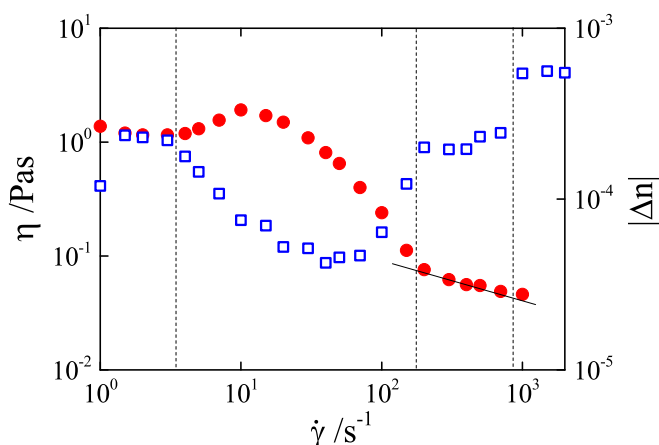


Fig. 3 Viscosity and birefringence intensity as a function of shear rate for the sample with $B/H = 0.34$ at 25°C . Vertical dotted lines indicate characteristic shear rates. Symbols are the same as those in Fig. 1. The first dotted line at low shear rate corresponds to the formation of the onion phase. The second dotted line in the intermediate shear rate indicates the rupture of the onion phase (i.e., the recovery of the lamellar phase), and the third one at high shear rate corresponds to the transition in orientation from parallel to perpendicular. The solid line shows the power law relation with a slope of $-1/3$, $\eta \sim \dot{\gamma}^{-1/3}$, which is identical to the theoretically predicted value.

Newtonian behavior in the perpendicularly oriented layers has also been reported for some systems^{13,18,40}. As the shear rate is increased further, the degree of orientation seems to be enhanced, as indicated by the increase in peak.

In contrast to the sample with $B/H = 0.30$, the data sets for the system with $B/H = 0.34$ show different features. At low shear rate, shear-thickening behavior with the critical shear rate $\dot{\gamma}_c = 4 \text{ s}^{-1}$ is observed. As has been observed for many surfactant lamellar phases, the shear-thickening behavior is often associated with shear-induced onion phase formation^{1,3,5–7,12,15}. The flow birefringence intensity $|\Delta n|$ simultaneously starts to decrease as the shear-thickening appears. The reduction in $|\Delta n|$ is also reasonable if a structural transition of the lamellae from aligned to isotropically curved proceeds. Thus, these rheological and optical behaviors suggests that the onion phase forms at the shear rate above $\dot{\gamma}_c = 4 \text{ s}^{-1}$. Onion phase formation in the system with $B/H = 0.34$ was identified by rheo-SALS and SAXS experiments in Fig. 4. The four-leaf pattern that appeared in the rheo-SALS pattern above shear rates of $\dot{\gamma}_c = 4 \text{ s}^{-1}$ is representative of the shear-induced onion phase^{5–7}. Furthermore, the isotropically curved layers in the onion structure are also detected as isotropic Bragg scattering in the rheo-SAXS at $\dot{\gamma} = 10, 30, \text{ and } 100 \text{ s}^{-1}$. These features

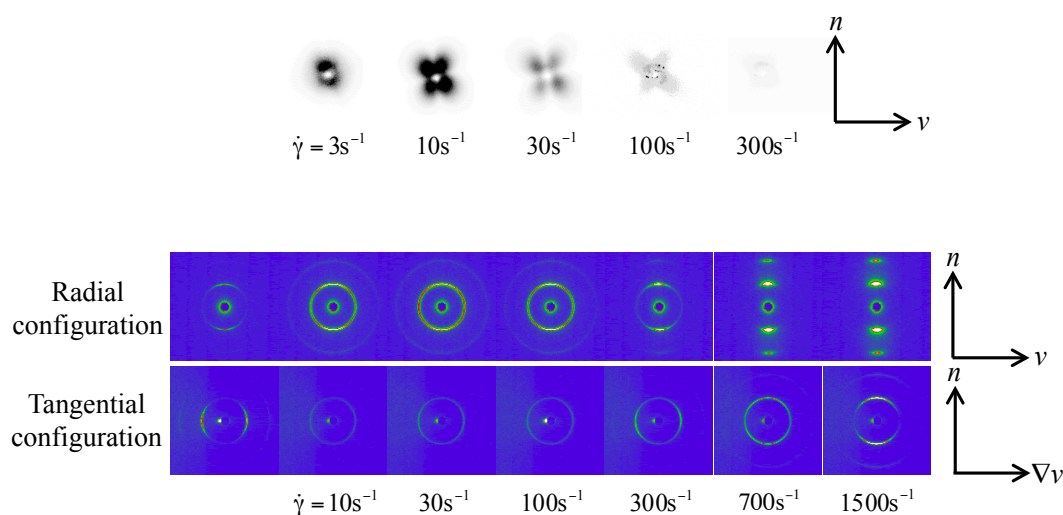


Fig. 4 Rheo-SALS (upper) and rheo-SAXS (bottom) patterns obtained for the same system used in Fig. 3. In the rheo-SALS patterns, the vertical and horizontal directions correspond to the neutral (n) and flow (v) directions, respectively. In the rheo-SAXS pattern, the scattering patterns in the neutral (n)-flow (v) planes (radial configuration) and the neutral (n)-velocity gradient (∇v) planes (tangential direction) are shown. The SAXS pattern on the left end was obtained before shearing. In each image, the corresponding shear rate is shown at the bottom of the image.

demonstrate that the onion phase was consistently formed. After the shear-induced onion phase formation, shear-thinning viscosity is observed in a wide shear rate region $\dot{\gamma} > 10 \text{ s}^{-1}$. The slope of the shear-thinning changes at $\dot{\gamma} = 200 \text{ s}^{-1}$. At shear rates higher than $\dot{\gamma} = 200 \text{ s}^{-1}$, the viscosity follows a power law behavior as $\eta \sim \dot{\gamma}^{-1/3}$, which is the same as that observed in Fig. 1. In the same shear rate region, $|\Delta n|$ recovers to the same level as that before the onion phase formation below $\dot{\gamma}_c = 4 \text{ s}^{-1}$. The increase in $|\Delta n|$ indicates the breakup of the onion structure and reformation of the planar lamellar phase. The disappearance of the four-leaf pattern at $\dot{\gamma} = 300 \text{ s}^{-1}$ in the rheo-SALS pattern also suggests the rupture of the onion structure. The SAXS profile at $\dot{\gamma} = 300 \text{ s}^{-1}$ indicates the presence of the $L_\alpha(\text{C})$ phase. As the shear rate is further increased, $|\Delta n|$ suddenly increases, as observed in the system with $B/H = 0.30$. After the jump, the level of $|\Delta n|$ reaches the same intensity as that for $B/H = 0.30$, suggesting that the planar lamellae undergoes an orientation transition. As one can see at $\dot{\gamma} = 1500 \text{ s}^{-1}$, the anisotropic Bragg peaks along the n directions in both the radial and tangential configurations clearly prove that the orientation state is $L_\alpha(\text{A})$ phase. **Although we could not observe the Newtonian behavior in the shear rate range of the viscometry, the viscosity gradually levels off at $\dot{\gamma} = 1000 \text{ s}^{-1}$, suggesting the appearance of Newtonian behavior.** Thus we conclude that this systems show several orientation transitions as a function of shear rate: $L_\alpha(\text{C})$ /onion transition, melting of the onion structure into $L_\alpha(\text{C})$, and $L_\alpha(\text{C})/L_\alpha(\text{A})$ transition.

Here, we would like to point out appearance of the isotropic Bragg ring in the tangential configuration at $\dot{\gamma} = 700 \text{ s}^{-1}$. As mentioned above, the isotropic Bragg ring suggests the presence of isotropically curved lamellae. We have confirmed that the same SAXS profile also appears at the critical shear rate of the $L_\alpha(\text{C})/L_\alpha(\text{A})$ transition in other samples (see Fig. 3 in the supplemental information).

The experimental results shown above are typical samples showing orientation transitions. The orientation behaviors we observed are essentially the same as those of the same block copolymer lamellar systems studied by Richter *et al.*^{13,15}. The primary contributions of our study are the findings of the rupture of the onion phase and the orientation transition after the rupture at high shear rate. Note that the rheological and optical properties are crucial for detecting the structural and orientation transitions of lamellae even without rheo-SALS and rheo-SAXS.

The polarized microscopy images of samples with $B/H = 0.30$ and 0.34 at $T = 25 \text{ }^\circ\text{C}$ are shown in Fig. 5. Both samples have oily streak defects; however, the thickness and orientation of the oily streaks obviously depend on the solvent composition. At $\dot{\gamma} = 3 \text{ s}^{-1}$, the oily streaks in the sample with $B/H = 0.30$ are much thicker than those in the sample with $B/H = 0.34$. The oily streaks orient along the v direction and become thinner as the shear rate increases. One can see a hazed texture at $\dot{\gamma} = 100 \text{ s}^{-1}$ resulting from the fine structures of the defects. The orientation transition into the $L_\alpha(\text{A})$ phase should

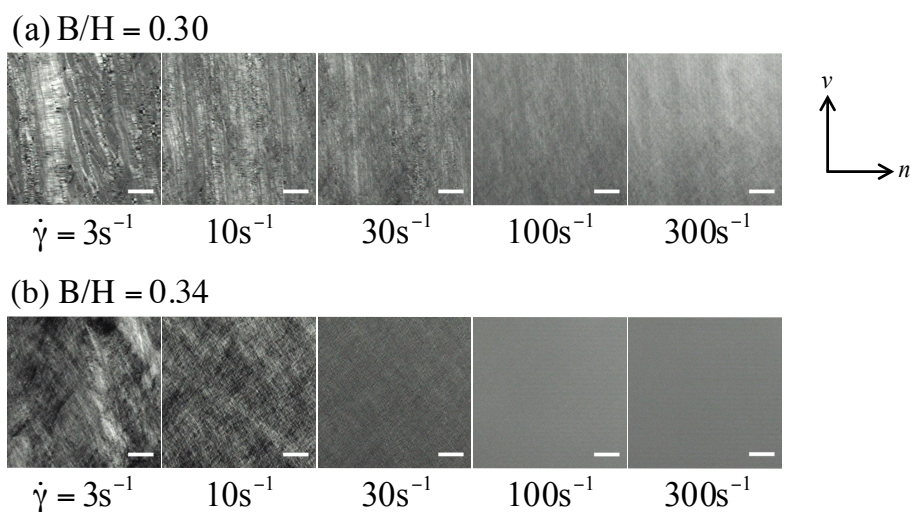


Fig. 5 Polarized microscopy images of samples with (a): $B/H = 0.30$ and (b): $B/H = 0.34$ at $25\text{ }^{\circ}\text{C}$. Scale bars are $100\text{ }\mu\text{m}$.

be induced at $\dot{\gamma} = 300\text{ s}^{-1}$, due to the resolution of the optical microscope, it is difficult to see the defects and mesoscale structures. On the other hand, at $B/H = 0.34$, the oily streaks are rather thin and orient 40° from the v direction and form a defect network. At $\dot{\gamma} = 10\text{ s}^{-1}$, the densely packed onion phase is recognized. The size of the oily streaks decreases with the shear rate, as has been reported for many surfactant systems. At $\dot{\gamma} = 100\text{ s}^{-1}$, one cannot identify the onion structure due to resolution limitations of the optical microscope. Finally at $\dot{\gamma} = 300\text{ s}^{-1}$, where the $L_{\alpha}(C)$ phase should be recovered, no defects such as oily streaks are observed. Although it is difficult to determine the structure at high shear rate (i.e., the defects and onion phase) are consistent with the above experimental results. The dependence of the thickness of the oily streak on solvent composition represents the change in the elastic properties of the lamellae³⁹.

It is well recognized that defects dominate the rheological properties of the lamellar phase^{36–38,41–43}. In particular, the shear-induced onion phase seems to be strongly related to defects¹². On the basis of shear modulus measurements, Medronho *et al.* reported that an increase in defect density is a necessary precursor to onion phase formation⁴³. On the other hand, Dhez *et al.* qualitatively suggested that the length of screw dislocation determines the threshold of shear-induced onion phase formation²⁰. As we observed, the differences in the thickness of the oily streak and orientation direction may affect the structural transition under shear.

3.2 Dynamic orientation diagram

The experimental results are summarized in the form of a dynamic orientation diagram as functions of B/H and shear rate in Fig. 6. The left panel shows the orientation diagram at $T = 25\text{ }^{\circ}\text{C}$. Here, the subscripts U and L in $L_{\alpha}(C)$ indicate the upper and lower $L_{\alpha}(C)$ phase, respectively. At low B/H , no onion phase formation occurs while only the $L_{\alpha}(C)/L_{\alpha}(A)$ orientation transition is observed at high shear rate. Above $B/H = 0.325$, the onion phase appears in the middle shear rate range, followed by the rupture of the onion phase at shear rates over 100 s^{-1} and the recovery of the $L_{\alpha}(C_U)$ phase. A further increase in shear rate induces the $L_{\alpha}(C_U)/L_{\alpha}(A)$ orientation transition. The rupture of the onion structure and thus the recovery of the $L_{\alpha}(C)$ phase were also reported by Roux *et al.*¹. They reported that the $L_{\alpha}(C_U)$ phase at high shear rates has perfectly aligned lamellae without defects.

In the right panel, the dynamic orientation diagrams at different temperatures are compared. The dynamic orientation state of this system significantly depends on the temperature. While no onion phase formation was confirmed at $T = 21\text{ }^{\circ}\text{C}$, the onion phase region expands as temperature increases. At $T = 27\text{ }^{\circ}\text{C}$, the onion phase is easily formed at low shear rate over wide B/H value. The $L_{\alpha}(C)/L_{\alpha}(A)$ orientation transition in the high shear rate region also depends on temperature, and the critical shear rate increases with temperature. Surprisingly slight differences in temperature significantly affect the dynamic orientation state. The origins of these critical shear

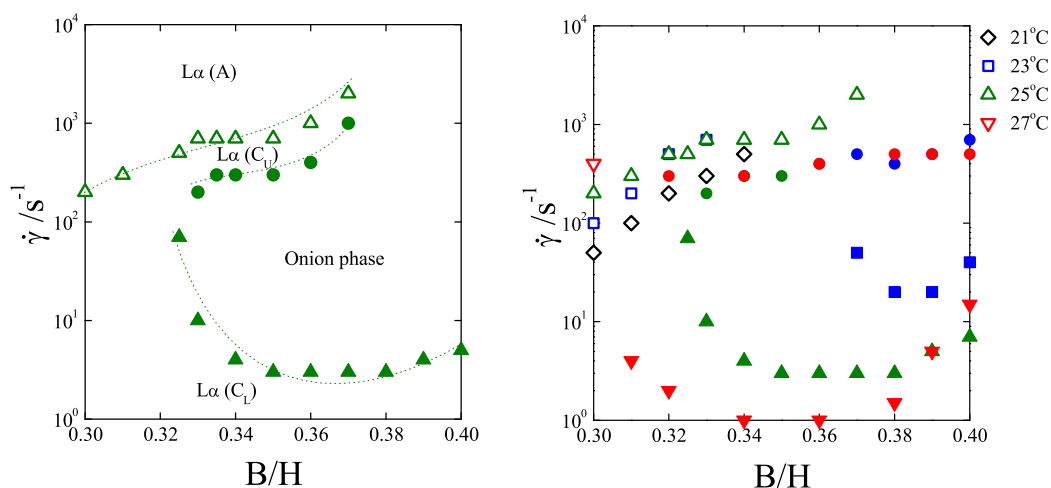


Fig. 6 Left: dynamic orientation diagram at 25 °C as a function of B/H and shear rate. Closed triangles correspond to the critical shear rate of the $L_\alpha(C)$ /onion transition. Closed circles correspond to the rupture of the onion phase and the onion/ $L_\alpha(C)$ transition. Open triangles indicate the $L_\alpha(C)/L_\alpha(A)$ transition. The subscripts U and L in $L_\alpha(C)$ indicate the upper and lower $L_\alpha(C)$ phases, respectively. Right: dynamic orientation diagrams at different temperatures (black, 21 °C, blue, 23 °C, green, 25 °C, and red, 27 °C). Different symbols with different colors at the lower shear rate correspond to the critical shear rate of the onion phase formation. Closed circle with different colors at high shear rate corresponds to the characteristic shear rate of the rupture of the onion phase. Open symbols correspond to the critical shear rate for the $L_\alpha(C)/L_\alpha(A)$ orientation transition.

rates, the $L_\alpha(C)/L_\alpha(A)$ orientation transition, and the rupture of the onion structure will be considered later.

3.3 Characterization of the $L_\alpha(C)$ phase

The dynamic orientation diagram suggests that the onion phase can be formed from the $L_\alpha(C)$ phase at both high and low shear rates. In Fig. 7, the transient viscosities during the onion phase formation from the $L_\alpha(C_L)$ and the $L_\alpha(C_U)$ phases are shown. Here, the system with $B/H = 0.38$ was used for the measurements at $T = 23$ °C. The initial conditions of $L_\alpha(C_L)$ and $L_\alpha(C_U)$ phases were prepared at $\dot{\gamma} = 1$ and 2000 s^{-1} , respectively. A shear rate of $\dot{\gamma} = 100 \text{ s}^{-1}$ was then applied as a step function. In the shear jump test, as $\dot{\gamma}$ is increased to from 1 s^{-1} to 100 s^{-1} , the viscosity increases in two steps and reaches the steady state. On the other hand, in the shear quench test, after quenching the shear rate from $\dot{\gamma} = 2000 \text{ s}^{-1}$ to 100 s^{-1} , the viscosity is increased and eventually approaches to the same value as the viscosity in the shear jump test. In previous studies, we found that the first step in the viscosity growth can be attributed to the increase in defect density; the second step is attributed to the appearance of the onion phase^{5,12}. Qualitatively, the similar behavior observed for both the shear jump experiment from the $L_\alpha(C_L)$ phase and the shear quench experiment from the $L_\alpha(C_U)$ phase in-

dicates that the onion phase formation proceeds via the same process. However, the growth in viscosity in the shear quench experiment is delayed compared with that in the shear jump experiments. The $L_\alpha(C_U)$ phase at high shear rate is considered to have perfectly aligned lamellae without defects^{1,27}. The delay in the increase in viscosity is this attributed to the absence of defects in the $L_\alpha(C_U)$ phase. The $L_\alpha(C_U)$ phase with fewer defects require more time to develop defects. The shear quench behavior indirectly supports the existence of the $L_\alpha(C_U)$ phase with few defects at high shear rates. **Please note that the slight inhomogeneity of the shear cell is sufficient to induce dislocation, even if the inhomogeneity is on the nano-meter scale²⁷.** As shown in Fig. 5(b), the $L_\alpha(C_L)$ phase exhibits oily streak defects at low shear rates, while no such defects can be identified at $\dot{\gamma} = 300 \text{ s}^{-1}$ under the optical microscope. Each planar lamellae in the $L_\alpha(C_L)$ and $L_\alpha(C_U)$ phases are characterized by a large difference in the defect density.

4 Discussion

We found three orientation transitions in above experiments. At low shear rate, samples with higher B/H values showed shear-induced onion phase formation. In contrast, at high shear rates, the onion phase was ruptured into the $L_\alpha(C)$

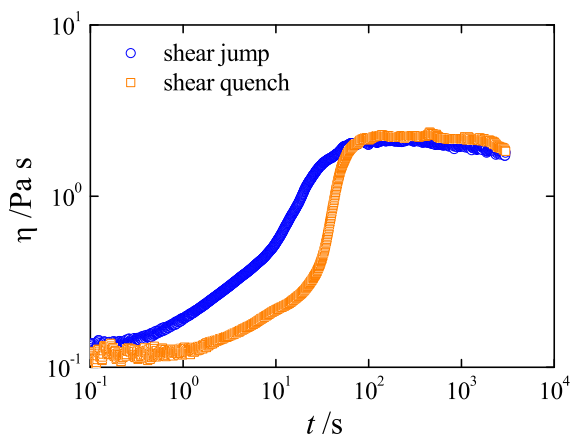


Fig. 7 Comparison of onion phase formation behavior from different states at $\dot{\gamma} = 100 \text{ s}^{-1}$. The solvent composition is $B/H = 0.38$, and the measurement temperature is $T = 23 \text{ }^\circ\text{C}$. Transient viscosity was measured by increasing the shear rate from the $L_\alpha(C_L)$ phase at $\dot{\gamma}_i = 1 \text{ s}^{-1}$ (shear jump) or quenching shear rate from the $L_\alpha(C_U)$ phase at $\dot{\gamma}_i = 2000 \text{ s}^{-1}$ (shear quench).

phase, and the orientation transition from the $L_\alpha(C)$ phase to the $L_\alpha(A)$ phase occurred in a wide range of B/H . We refer to each transition as the onion/ $L_\alpha(C)$ transition and the $L_\alpha(C)$ / $L_\alpha(A)$ orientation transition with critical shear rates of $\dot{\gamma}_{\text{max}}$ and $\dot{\gamma}_{\text{c/a}}$, respectively. In this section, we focus on the orientation transitions at high shear rate, which are poorly understood compared with the onion phase formation.

4.1 Critical condition of the orientation transition

As we have shown, different orientation states can be observed at the same solvent composition when the shear rate is increased. In this section we consider critical conditions of those transitions. The lyotropic lamellar phase has several relaxation modes such as undulation, baroclinic, and sound mode^{44–46}. Among those relaxation modes, the baroclinic mode is the slowest one³². Lu indicated that the decay rate of the baroclinic mode $\Gamma \sim \mu \bar{B} l(l+1)/r_n^2$ with low deformation mode l almost coincides with the critical shear rate of onion formation^{32,47}. Here, μ is the squeezing mobility between two membranes given by $\mu = (d - \delta)^2/12\eta_s$ with solvent viscosity η_s , repeating distance d and membrane thickness δ ⁴⁴. \bar{B} and r_n are the compression modulus and radius of the onion, respectively. Lu calculated a dynamic free energy density with the baroclinic mode dispersion relation and found that the scaling behavior of the onion size is determined by the free energy minima. This implies that the mode for squeezing water between two layers is responsible of the relaxation of

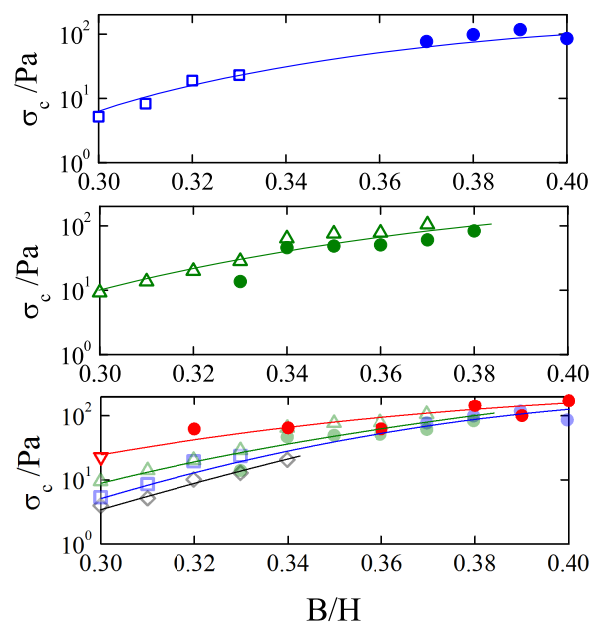


Fig. 8 Stress at the critical shear rates of the $L_\alpha(C)/L_\alpha(A)$ orientation transition ($\dot{\gamma}_{\text{c/a}}$) and the onion/ $L_\alpha(C)$ transition ($\dot{\gamma}_{\text{max}}$) as a function of B/H at different temperatures: (a) $23 \text{ }^\circ\text{C}$, (b) $25 \text{ }^\circ\text{C}$ and (c) $27 \text{ }^\circ\text{C}$. Stress σ was estimated from the η of the system at critical shear rate instead of the solvent viscosity. Solid curves are the guides for the eyes. In panel (c), all data of the critical stress σ_c at $T = 21, 23,$ and $25 \text{ }^\circ\text{C}$ are plotted for reference.

the onion structure. In addition, the characteristic shear rate for the rupture of the onion structure was also predicted on the basis of the disappearance of the minima where the onion size is close to the core size ($\sim d$). Interestingly, the theory is in good agreement with the experiments performed by Roux *et al.* The maximum shear rate at which the onion structure disappears is given by

$$\dot{\gamma}_{\text{max}} = \frac{6\mu\bar{B}}{(13.1\lambda)^2}, \quad (1)$$

where $\mu\bar{B}$ is the dimension of diffusivity, and the smectic penetration length λ is close to the core size ($\sim d$). The onion formation and its rupture are both closely related to the dynamic balance between the internal relaxation mode of the lamellae and external shear. The baroclinic mode dispersion relation is similar to that of the permeation mode, $\mu\bar{B}q_x^2$.

On the other hand, the theoretically argued mechanism of the orientation transition is based on the undulation mode which is affected by shear^{25–27}. The lyotropic lamellar phase is stabilized by steric repulsion resulting from the undulation fluctuation^{45,46}. However, the shear flow will iron out the

membranes and suppress the undulation mode with a long wavelength amplitude fluctuation. The reduction of the entropic repulsive force results in instability, causing the layers to realign. The critical shear rate of the orientation transition predicted by Ramaswamy is²⁵

$$\dot{\gamma}_{c/a} = \frac{(k_B T)^3}{\eta_s \kappa^2 d^3}. \quad (2)$$

Here, k_B is the Boltzmann constant, T is the temperature, and κ is the rigidity constant of the membrane. Al kahwaji *et al.* confirmed that the validity of the theory was experimentally confirmed for the lamellar phase of the ionic surfactant AOT¹⁹. However, note that good agreement with theory is obtained only when the zero-shear viscosity η_0 is incorporated instead of η_s .

Considering the ratio of these critical shear rates under the assumption of $\kappa \propto k_B T$ and $\lambda \propto d$, the difference in the time scales of these transitions can be attributed to the viscosity and lamellar spacing, $\dot{\gamma}_{c/a}/\dot{\gamma}_{\max} = 247.5(\eta_s/\eta)(d-\delta)^2/d^2$. In this study, the value of $(d-\delta)^2/d^2$ is estimated to be 0.6¹³. The ratio of two critical shear rates thus depends only on the viscosity. The above relation can be further reduced to $\dot{\gamma}_{c/a}\eta \simeq 150\dot{\gamma}_{\max}\eta_s$. At the maximum shear rate where the onion phase disappears, the viscosity is roughly 100 mPas. Thus taking the viscosity instead of η_s offsets the pre-factor in the above relation, suggesting that the shear stress at the transition point has almost the same value, $\sigma_{c/a}/\sigma_{\max} \sim O(1)$. The critical shear stresses at the orientation transition point and at the rupture of the onion phase were compared in Fig. 8. Both critical stresses collapse onto the same curve, especially at $T = 25^\circ\text{C}$, where they are almost coincidental. Under stress controlled experiments, the coexistence of $L_\alpha(A)$ and the onion phases is expected. The occurrence of different structural transitions at the same stress value suggests that all structural transitions in the lamellar system are driven by a balance of two forces: viscous force applied by shear and the internal relaxation mode of lamellae, which depends on the elastic properties of the membrane. This conclusion is similar to Taylor's argument in the droplet problem^{48–50}. At the maximum shear rate, viscous stress reaches to a critical value and prevails over the effective surface tension of the membrane, resulting in the breakup of the onion phase. The viscous stress decreases due to the disappearance of the onion phase. The membranes will again become unstable when the viscous stress approaches the critical value, and the orientation transition will consequently occur as the second transition.

Here we consider if the critical shear stress is related to the change in d with solvent composition and temperature. Fig. 9 shows the typical SAXS profiles for samples with different B/H values at a shear of $\dot{\gamma} = 10\text{ s}^{-1}$ and $T = 25^\circ\text{C}$. The lamellar spacing d obtained from the SAXS profiles are also shown as a function of temperature. The temperature de-

pendence of the lamellar spacing d changes with the solvent composition. At $B/H = 0.30$, d increases with temperature while it does not show significant temperature dependence at $B/H = 0.38$. At fixed temperature, d decreases with increasing in butanol content. Previously, Zipfel *et al.* reported that the increase in butanol content reduces the lamellar spacing d because of the slight decrease in the apolar thicknesses of the lamellar membranes; in contrast, d increases with temperature due to the increase in the apolar thickness caused by the change in the solubility of each block and the hydration of the EO block¹³. These experimental findings are similar to our results with the exception of the temperature dependence of d for samples with higher butanol content; our results suggested that for $B/H > 0.34$, d does not depend on temperature. Comparing the B/H dependences of σ_c and d , σ_c increases with decreasing d . In contrast, the temperature dependence of σ_c increases with d . Thus their tendency in B/H and temperature dependences are inconsistent with each other. Their inconsistency suggests that the critical stress is not simply scaled by eq. 2 considering the change in d . In fact, we confirmed that the scaling behavior $\sigma_c \sim d^{-3}$ does not hold in this study. Previously we found that the critical stress of the onion phase formation is scaled by considering the bending rigidity of the lamellae¹². Adding cosurfactant into the surfactant system is known remarkably influence the elastic properties of bilayer membranes⁵¹. As reported by Zipfel *et al.*, butanol is interfacial active molecule and behaves as a cosurfactant. Butanol can insert in the interfacial region and stuck into hydrophobic part of the membranes. The sticking of butanol to the membranes changes the elastic properties, and slight changes in sample composition lead to significant differences in the dynamic orientation state under shear.

4.2 Possible scenario of the orientation transition

The origin of the orientation transition has been attributed to the suppression of the undulation fluctuation based on theory^{25–27,31}. In the theory developed on the basis of the shear effect on the Helfrich interaction, the lamellar spacing is reduced in the vicinity of the transition point as a result of the suppression of the undulation fluctuation. There have been several discussions and reports on the shear effect of the lamellar spacing^{10,19,52,53}. However, we did not observe the reduction of the lamellar spacing at the critical shear rate (Figs. 1 and 2 in Supplemental Information). As we have shown in Fig. 5(a), the $L_\alpha(C)$ phase includes many oily streak defects. **In general, the shear flow generates more defects to relieve the imposed strain. Hence it is necessary to consider the influence of the defects on the orientation transition.**

The influence of the defects on the rheology has been discussed in several studies^{36–38}. The power law relation of

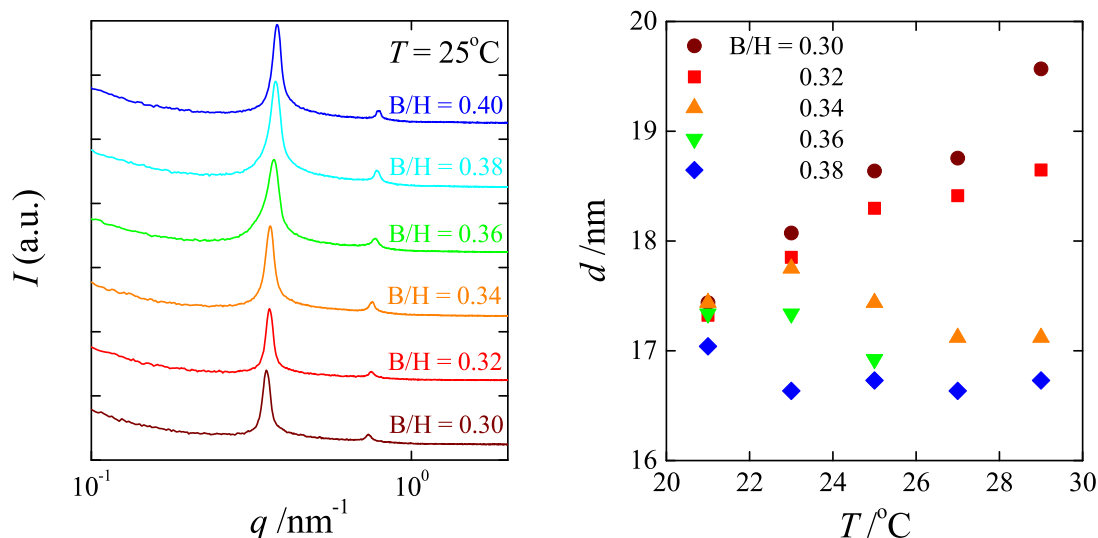


Fig. 9 Figure on the left: SAXS profiles obtained for samples with different solvent composition B/H under shear of $\dot{\gamma} = 10 \text{ s}^{-1}$ at $T = 25^{\circ}\text{C}$. SAXS profiles are vertically shifted for the eyes. Figure on the right: lamellar spacing d obtained for samples with a different B/H as a function of temperature.

the shear-thinning $\eta \sim \dot{\gamma}^{-1/3}$ in Figs. 1 and 3 suggests that the nonlinear rheology in this system is dominated by the nucleation-annihilation dynamics of dislocations as proposed by Lu *et al.*³⁸. This also means that in the shear rate region where the nucleation-annihilation dynamics are dominant, the dislocations can move with the flow. Dislocation movement is driven by the Peach-Koehler force, and its velocity is proportional to the shear stress $v = M\sigma$ ⁶⁰. M is the mobility of the dislocations and is usually given by ($M = v/\sigma = 10^5 \text{ m}^2\text{kg}^{-1}$) in the lyotropic lamellar phase⁶¹. However, at high shear rates, dislocations are no longer able to follow the flow²⁹. In this limit, inhomogeneous lamellar spacing around the dislocations will destabilize the system because dilation develops at the same time. To keep the lamellar spacing constant, the system must find another alignment to be able to flow. This might be the critical shear rate where the orientation transition appears. Using a critical shear stress of $\sim 10^2 \text{ Pa}$, we simply estimated the limiting velocity of the dislocations to be $v = 10^7 \text{ m/s}$. By dividing the limiting velocity by the sample thickness ($\sim 10^2 \mu\text{m}$), the shear rate at the limiting velocity is estimated to be $\dot{\gamma}_{\text{lim}} \sim 10^2 - 10^3 \text{ s}^{-1}$, which almost corresponds to the critical shear rate. Thus the origin of the critical shear rate might be the limiting velocity of the dislocations driven by shear stress. Scaling behavior of the critical shear stress in Fig. 8 suggested that the structural transitions are driven by a balance between viscous force and the internal relaxation mode of the lamellae. The limiting velocity of defects might be controlled by the internal relaxation mode.

The thermotropic smectic phase also shows the orientation

transition with increasing shear rate, despite the high density of oily streak defects^{18,40}. As far as we know, there is no clear experimental evidence for the shear rate dependence of the layer spacing in the thermotropic smectic phase. Previously, we found that the critical shear rate of the orientation transition in the smectic phase drastically decreases in the vicinity of the smectic/nematic transition point, where the defect size is diversely increased. In the case of such a high defect density, the orientation transition might be associated with defect rearrangement⁵⁵. Dhez *et al.* reported that the dislocation size is correlated with the onion phase formation and orientation transition²⁰.

4.3 Intermediate structure in the orientation transition

In this section, we highlight the presence of an intermediate structure at the orientation transition point from the $L_{\alpha}(\text{C})$ phase to the $L_{\alpha}(\text{A})$ phase. The SAXS profile as a function of shear rate is shown in Fig. 4. The SAXS profile with a sharp Bragg peak in the radial configuration at $\dot{\gamma} = 700 \text{ s}^{-1}$ indicates a highly oriented lamellar phase with the layer normal along the n direction. On the other hand, the isotropic Bragg ring in the tangential configuration indicates the presence of curved lamellae. To obtain information about the orientation of the lamellae, the SAXS profiles in Fig. 4 are plotted as an azimuthal angle dependence of the intensity at specific wavelength at which the SAXS profile shows the peak in the intensity. We follow the method of Picken *et al.*⁵⁶ and quantify the degree of orientation of the lamellar phase. Picken *et al.* described the azimuthal intensity profile by the following re-

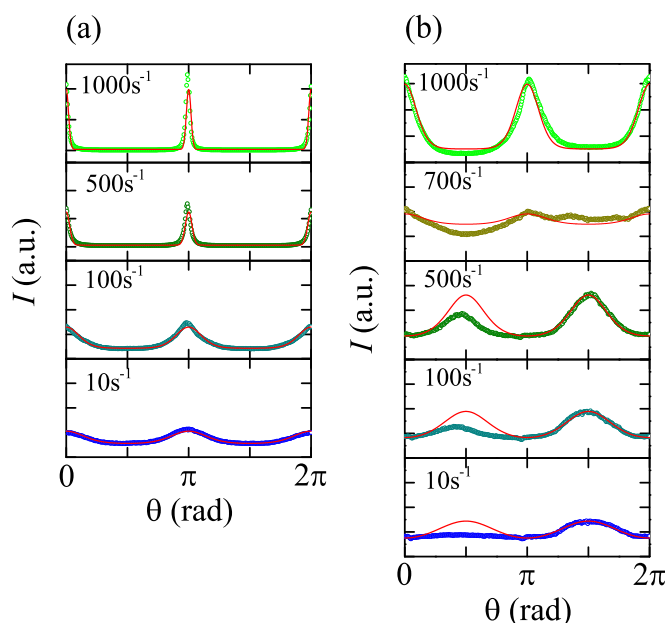


Fig. 10 SAXS intensity as a function of the azimuthal angle θ in the radial (a) and tangential (b) configurations at several shear rate. In the radial and tangential configuration, $\theta = \pi/2$ corresponds to the v and ∇v directions, respectively. The azimuthal intensity profile was obtained from the SAXS images shown in Fig. 4. The solid lines are the best fits obtained using eq. 3.

lation, which assumes a Maier-Saupe type of orientation distribution function

$$I(\theta) = I_0 \exp[\alpha(P_2(\cos\theta) - 1)] + I_c, \quad (3)$$

where $P_2(x)$ is the Legendre polynomial of variable x and α is the distribution parameter that characterizes the width of the intensity profile^{56,57}. I_0 and I_c are the maximum intensity and background contribution to the azimuthal profile, respectively. The orientational parameter S of the lamellar phase is determined as the numerical integration of

$$S = \frac{\int_{-1}^1 \exp[\alpha P_2(\sin\theta)] P_2(\sin\theta) d \sin\theta}{\int_{-1}^1 \exp[\alpha P_2(\sin\theta)] d \sin\theta}. \quad (4)$$

The scattering intensity in the radial configuration (Fig. 10(a)) develops a maxima at $\theta = 0$ and π monotonically with increasing $\dot{\gamma}$. In contrast, in the tangential configuration (Fig. 10(b)), a scattering intensity with maxima at $\theta = 1/2\pi$ and $3/2\pi$ also develops with increasing $\dot{\gamma}$. However, at $\dot{\gamma} = 700 \text{ s}^{-1}$, the amplitude is suddenly reduced indicating that the lamellae are randomly oriented. As $\dot{\gamma}$ is further increased to 1000 s^{-1} , a scattering intensity with maxima at $\theta = 0$ and π develops due to the orientation transition. These azimuthal intensity profiles are well fitted by eq. 3, except for at $\dot{\gamma} = 700 \text{ s}^{-1}$. Here, we should note that the asymmetric profile in the

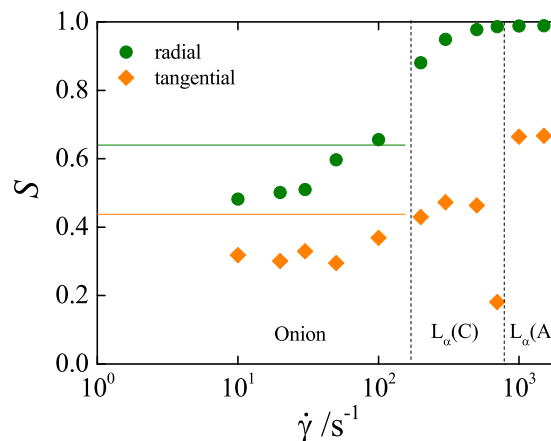


Fig. 11 Orientational parameter as a function of shear rate for the system with $B/H = 0.34$. Horizontal solid lines correspond to the orientational parameter before shearing. Vertical dotted lines show $\dot{\gamma}_{\max}$ and $\dot{\gamma}_{c/a}$.

tangential configuration is derived from the curvature effect of the shear cell. Thus, the intensity profile in the range of $\pi < \theta < 2\pi$ was used for the fitting. The orientational parameter S estimated by numerical integration of eq. 4 is plotted as a function of $\dot{\gamma}$ in Fig. 11. The horizontal lines indicate the value of S before shearing. In the shear rate domain below 200 s^{-1} , which corresponds to the onion phase region, the value of S is lower than that before shearing. With increasing $\dot{\gamma}$, S increases with a sigmoidal curve indicating that the lamellae start to orient collectively because of the rupture of the onion phase. After the reformation of the planar $L_\alpha(C)$ phase, S in the radial configuration reaches almost 1. On the other hand, S in the tangential configuration suddenly decreases at $\dot{\gamma} = 700 \text{ s}^{-1}$. The value of S in the radial and tangential configurations suggest that the lamellae are highly oriented along the flow direction, while their orientations along ∇v are almost random at the transition point. After the transition into the $L_\alpha(A)$ phase, S increases dramatically to $S \simeq 0.65$, indicating a relatively higher orientation of the lamellae along the ∇v direction. For more detailed kinetic information, it is necessary to perform rheo-SAXS experiments with small shear rate steps in the vicinity of the transition point. Other complementary methods such as rheo-NMR spectroscopy are also expected to be useful for the detection of intermediate structures; for example, Medronho *et al.* studies the formation of the shear-induced onion phase⁵⁸.

The orientational parameter and SAXS profiles suggest several possibilities for the state of the orientation; these include coherently buckled lamellae with a characteristic wavelength or multilamellar cylinder structures. A Bragg ring with low

S may appear even in the defective lamellar phase filled with oily streak defects. However, the absence of the oily streak defects confirmed by optical microscopy suggests that this is not the case. One might also consider the possibility of the coexistence of the $L_{\alpha}(C)$ and $L_{\alpha}(A)$ phases. In this case, we expect mixed Bragg peaks along the n and ∇v directions but not the isotropic ring reported for the block copolymer lamellar phase²⁴. We confirmed that the same SAXS profile appeared in the $L_{\alpha}(C)/L_{\alpha}(A)$ orientation transitions of other samples with different B/H ratios (Fig. 3 in Supplemental Information). Similar scattering profiles have been observed during the transient process of shear-induced onion phase formation⁵. We should note that this characteristic SAXS profile was observed at a steady state but not during the transient process. Rheo-SAXS profiles indicate the presence of a steady state intermediate structure. A stable intermediate phase region with a very narrow shear rate domain would exist. To our best knowledge, this is the first report of a stable intermediate structure in the orientation transition. **The results of molecular dynamics simulation performed by Guo suggest the formation of the intermediate structure⁵⁴. In the simulation, the undulation fluctuation along the flow direction was suppressed by shear flow. Since the undulation fluctuation along the neutral direction is not coupled to the shear flow, lamellae break up into mono-domains along the neutral direction. The fragmented lamellar domain then rotates into the perpendicular orientation and organizes the perpendicularly oriented lamellar phase by migration and annihilation of the defects.** The rotation of the lamellar mono-domain due to the decoupling of the undulation fluctuation along the direction neutral to the shear flow might be the origin of the steady state intermediate structure formation. It is interesting that Shiba *et al.*, first reproduced the rolled structure of the lamellae in their simulation study⁵⁹. Their simulation results suggest that the multilamellar cylinder is a plausible intermediate structure. **These simulations results are not inconsistent with rheo-SAXS experiments and orientational parameter analysis.**

Recently, Kato *et al.* found a stable intermediate structure between the lamellar and onion phase by rheo-SAXS measurement¹¹. Interestingly, they also found that the lamellae with perpendicular orientation are enhanced prior to the onion phase formation. The appearance of the orientation transition like behavior in the vicinity of the onion phase formation may imply that the intermediate structure formation is necessary for the non-equilibrium structural transition in the lamellar system despite the large difference in critical shear rate.

5 Conclusions

We have studied the dynamic orientation transitions of the lyotropic lamellar phase of Plutonic P123 block copolymer systems with different solvent composition. By combining vis-

cometry, birefringence, rheo-SALS and rheo-SAXS measurements, we have constructed the dynamic orientation diagram over a wide range of shear rates. The dynamic orientation diagram revealed that several orientation transitions are induced by increasing the shear rate, even at the same sample composition. At low B/H ratios, samples show only the $L_{\alpha}(C)/L_{\alpha}(A)$ orientation transition at high shear rate. In contrast, samples with high B/H ratios exhibit the shear-induced onion formation at low shear rates followed by a variety of orientation transitions including the reformation of the planar $L_{\alpha}(C)$ phase due to the rupture of the onion structure, and the $L_{\alpha}(C)/L_{\alpha}(A)$ orientation transition. By considering the shear stress at the transition points, we found that the critical condition for the rupture of the onion structure and the $L_{\alpha}(C)/L_{\alpha}(A)$ orientation transition coincide with each other. The consistency of the shear stress values at the transition points suggests that the structural transition of the lamellar phase is driven by the mechanical balance between the applied viscous force and the internal relaxation mode of the lamellae in a similar way to the Taylor's droplet problem. **Assuming the existence of the limiting velocity of defects, we could estimate the critical shear rate of the orientation transition, which is in good agreement with the experimental results.** We also identified a stable intermediate structure in the $L_{\alpha}(C)/L_{\alpha}(A)$ orientation transition, which had not been reported until now. The presence of the stable intermediate structure may be a universal feature in the pre-transition stage of the lamellar system.

SF thanks T. Takahashi for use of the rheometer equipped with small angle light scattering and flow birefringence apparatus. SF acknowledges the support from KAKENHI (Grant-in-Aid for Scientific Research (B)) Grant No. 25287107 from the Ministry of Education, Culture, Sports, Science and Technology of Japan.

References

- 1 O. Diat, D. Roux, and F. Nallet, *J. Phys. II France*, **3**, 1427-1452, (1993)
- 2 D. Roux, F. Nallet, and O. Diat, *EPL*, **24**, 53-58, (1993)
- 3 C. Oliviero, L. Coppola, R. Gianferri, I. Nicotera, and U. Olsson, *Colloids and Surfaces A: Physicochemical and Engineering Aspects*. **228**, 85-90. (2003)
- 4 J. Zipfel, F. Nettesheim, P. Lindner, T. D. Le, U. Olsson, and W. Richtering, *EPL*, **53**, 335-341. (2000)
- 5 F. Nettesheim, J. Zipfel, U. Olsson, F. Renth, P. Lindner, W. Richtering, *Langmuir*, **19**, 3603-3618, (2003)
- 6 L. Gentile, Manja A. Behrens, L. Porcar, P. Butler,

- N. J. Wagner, and U. Olsson, *Langmuir*, **30**, 8316-8325, (2014)
- 7 L. Gentile and C. Oliviero, and U. Olsson *J. Colloid Interface Sci.*, **367**, 537-539, (2012)
- 8 Y. Kosaka, M. Ito, Y. Kawabata, and T. Kato, *Langmuir*, **26**, 3835-3842, (2009)
- 9 M. Ito, Y. Kosaka, Y. Kawabata, and T. Kato, *Langmuir*, **27**, 7409-7409, (2011)
- 10 T. Kato, K. Miyazaki, Y. Kawabata, S. Komura, M. Fujii, and M. Imai, *J. Phys. Cond. Matt.*, **17**, S2923. (2005)
- 11 D. Sato, K. Obara, M. Iwahashi, Y. Kawabata, and T. Kato, *Langmuir*, **29**, 121-132, (2013)
- 12 S. Fujii, D. Mitsumasu, Y. Isono, and W. Richtering, *Soft Matter*, **8**, 5381-5390, (2012)
- 13 J. Zipfel, J. Berghausen, G. Schmidt, P. Lindner, P. Alexandridis, and W. Richtering, *Macromolecules*, **35**, 4046-4074, (2002)
- 14 S. Fujii, and Y. Yamamoto, *J. Biorheol.*, **28**, 55-60, (2014)
- 15 J. Berghausen, J. Zipfel, P. Lindner, and W. Richtering, *J. Phys. Chem. B*, **105**, 11081-11088, (2001)
- 16 S. Fujii, and W. Richtering, *Soft Matter*, **9**, 5391-5400, (2013)
- 17 S. Fujii, S. Komura, and C.-Y. D. Lu, *Materials*, **7**, 5146-5168. (2014)
- 18 P. Panizza, P. Archambault, and D. Roux, *J. Phys. II France*, **5**, 303-311, (1995)
- 19 A. Al kahwaji, and H. Kellay, *Phys. Rev. Lett.*, **84**, 3073-3076, (2000)
- 20 O. Dhez, F. Nallet, and O. Diat, *EPL*, **55**, 821-826, (2001)
- 21 G. H. Fredrickson, and F. S. Bates, *Annu. Rev. Mater. Sci.*, **26**, 501-550, (1996)
- 22 U. Wiesner, *Macromol. Chem. Phys.*, **198**, 3319-3352, (1997)
- 23 Z.-R. Chen, and J. A. Kornfield, *Polymer*, **39**, 4679-4699, (1998)
- 24 B. S. Pinheiro, and K. I. Winey *Macromolecules*, **31**, 4447-4456, (1998)
- 25 S. Ramaswamy, *Phys. Rev. Lett.*, **69**, 112-115, (1992)
- 26 S. W. Marlow, and P. D. Olmsted, *Eur. Phys. J. E*, **8**, 485-497, (2002)
- 27 A. S. Wunenburger, A. Colin, T. Colin, and D. Roux, *Eur. Phys. J. E*, **2**, 277-283, (2000)
- 28 A. G. Zilman, and R. Granek, *Eur. Phys. J. B*, **11**, 593-608, (1999)
- 29 P. Oswald, and S. Ben-Abraham, *J. de Phys.*, **43**, 1193-1197, (1982)
- 30 G. K. Auernhammer, H. R. Brand, H. Pleiner, *Phys. Rev. E*, **66**, 061707, (2002)
- 31 R. Bruinsma, and Y. Rabin, *Phys. Rev. A*, **45**, 994-1008, (1992)
- 32 C.-Y. D. Lu, *Phys. Rev. Lett.*, **109**, 128304, (2012)
- 33 P. Holmqvist, P. Alexandridis, B. Lindman, *J. Phys. Chem. B*, **102**, 1149-1158, (1998)
- 34 S. Fujii, and W. Richtering, *Eur. Phys. J. E*, **19**, 138-148, (2006)
- 35 T. Ueki, Y. Hiragi, M. Kataoka, Y. Inoko, Y. Amemiya, Y. Izumi, H. Tagawa, and Y. Muroga, *Bio. Phys. Chem.*, **23**: 115-124, (1985)
- 36 C. Meyer, S. Asnacios, C. Bourgaux, and M. Kleman, *Rheol. Acta*, **39**, 223-233, (2000)
- 37 C. Meyer, S. Asnacios, and M. Kleman, *Eur. Phys. J. E*, **6**, 245-253, (2001)
- 38 C.-Y. D. Lu, P. Chen, Y. Ishii, S. Komura, and T. Kato, *Eur. Phys. J. E*, **25**, 91-101, (2008)
- 39 P. Boltenhagen, O. Lavrentvich, and M. Kleman, *J. Phys. II France*, **1**, 1233-1252, (1991)
- 40 S. Fujii, Y. Ishii, S. Komura, and C.-Y. D. Lu, *EPL*, **90**, 64001, (2010)
- 41 R. G. Horn, and M. Kleman, *Ann. Phys.*, **3**, 229-234, (1978)
- 42 G. Basappa, Suneel, V. Kumaran, P. R. Nott, S. Ramaswamy, V. M. Naik and D. Rout, *Eur. Phys. J. B*, **12**, 269-276, (1999)
- 43 B. Medronho, M. Rodrigues, M. G. Miguel, U. Olsson, and C. Schmidt, *Langmuir*, **26**, 11304-11313, (2010)
- 44 P. G. de Gennes, and J. Prost, *The Physics of Liquid Crystals* Carendon Press, London, 1993.
- 45 W. Helfrich, *Z. Naturforsch.*, 33a, 305. (1978)
- 46 W. Helfrich, *J. Phys. (Paris)*, **39**, 1199-1208, (1978)
- 47 P. Panizza, D. Roux, V. Vuillaume, C.-Y. D. Lu, M. E. Cates, *Langmuir*, **12**, 248-252, (1996)
- 48 G. I. Taylor, *Proc. R. Soc. A*, **146**, 501-523, (1934)
- 49 E. van der Linden, and J. H. M. Droege, *Physica A*, **193**, 439-447, (1993)
- 50 E. van der Linden, W. T. Hogervorst, and H. N. W. Lekkerkerker, *Langmuir*, **12**, 3127-3130, (1996)
- 51 P. Boltenhagen, M. Kleman, and O. Lavrentvich, *J. Phys. II France*, **4**, 1439-1448, (1994)
- 52 J. Yamamoto, and H. Tanaka, *Phys. Rev. Lett.*, **74**, 932-935, (1995)
- 53 L. Porcar, G. G. Warr, W. A. Hamilton, and P. D. Butler, *Phys. Rev. Lett.*, **95**, 078302, (2005)
- 54 H. Guo, *J. Chem. Phys.*, **124**, 054902, (2006)
- 55 S. Fujii, S. Komura, and C.-Y. D. Lu, *Soft Matter*, **10**, 5289-5295, (2014)

-
- 56 S. J. Picken, J. Aerts, R. Visser, M. G. Northolt, *Macromolecules*, **23**, 3829-3854, (1990)
- 57 H. Hoekstra, J. Vermant, J. Meiws, T. Narayanan, *Langmuir*, **18**, 5695-5703, (2002)
- 58 B. Medronho, C. Schmidt, U. Olsson, M. G. Miguel, *Langmuir*, **26**, 1477-1481, (2010)
- 59 H. Shiba, H. Noguchi, G. Gommper, *J. Chem. Phys.*, **139**, 014702, (2013)
- 60 K. Peach, J. Koehler, *Phys. Rev.*, **80**, 436-439, (1950)
- 61 M. Allain, M. Kleman, *J. de Phys.*, **48**, 1799-1807, (1987)